INTERNATIONAL JOURNAL FOR NUMERICAL METHODS IN FLUIDS, VOL. 23, 819–846 (1996)

A DEPTH-INTEGRATED 2D COASTAL AND ESTUARINE MODEL WITH CONFORMAL BOUNDARY-FITTED MESH GENERATION

BINLIANG LIN

Department of Civil and Environmental Engineering, University of Bradford, West Yorkshire BD7 1DP, U.K.

AND

SIMON N. CHANDLER-WILDE

Department of Mathematics and Statistics, Brunel University, Uxbridge, Middlesex, U.K.

SUMMARY

Details are given of the development and application of a 2D depth-integrated, conformal boundary-fitted, curvilinear model for predicting the depth-mean velocity field and the spatial concentration distribution in estuarine and coastal waters. A numerical method for conformal mesh generation, based on a boundary integral equation formulation, has been developed. By this method a general polygonal region with curved edges can be mapped onto a regular polygonal region with the same number of horizontal and vertical straight edges and a multiply connected region can be mapped onto a regular region with the same connectivity. A stretching transformation on the conformally generated mesh has also been used to provide greater detail where it is needed close to the coast, with larger mesh sizes further offshore, thereby minimizing the computing effort whilst maximizing accuracy. The curvilinear hydrodynamic and solute model has been developed based on a robust rectilinear model. The hydrodynamic equations are approximated using the ADI finite difference scheme with a staggered grid and the solute transport equation is approximated using a modified QUICK scheme. Three numerical examples have been chosen to test the curvilinear model, with an emphasis placed on complex practical applications.

KEY WORDS: shallow water equations; boundary-fitted co-ordinate systems; curvilinear meshes; finite difference method; conformal mapping

1. INTRODUCTION

Numerical methods as a tool for simulating flow and pollutant transport are increasingly important in hydraulic and environmental engineering. The two types of numerical models that are most commonly used in solving the two- dimensional (2D) depth-integrated shallow water equations are the finite difference method (FDM) and the finite element method (FEM). The FDM is simple to use and very effective in dealing with the non-linear advective terms in the shallow water equations, which may cause serious stability problems. Traditional finite difference models for shallow water flow and pollutant transport employ rectangular finite difference grids.[1,2] A disadvantage of this method is that the treatment of boundary conditions on curved boundaries is necessarily approximate,

CCC 0271–2091/96/080819–28

Received August 1995
Revised December 1995

with the curved boundary being replaced by a staircase of grid points. The FEM has the advantage of flexibility in dealing with problems of great geometrical complexity. Nevertheless, compared with the FDM, using the FEM, it is more difficult to reduce the numerical oscillation[3] and more expensive to invert the resulting matrices, which are generally very large.

Boundary-fitted co-ordinate systems provide an approach which combines the best aspects of finite difference methods, enabling more accurate resolution of the highly non-linear advective terms in the momentum and solute transport equations, e.g. with a greater degree of grid flexibility than regular grid schemes. In the last 10 years, several boundary-fitted curvilinear tidal circulation models have been developed, including those of Spaulding,[4] Hauser *et al.*,[5] Willemse *et al.*,[6] Shen *et al.*,[7] Gialone[8] and Borthwick and Barber.[9] With this method the physical curved region of flow is transformed onto a simpler computational domain on which the finite difference method is applied. In transforming the curved region to the computational domain, the governing equations of flow and solute transport are also transformed, thereby leading to more complex equations. The degree of complexity depends upon the type of the transformation, with the increase in the level of complexity being a disadvantage of this method.

Non-orthogonal co-ordinate transformations lead to the most complexity in the transformed equations. The advantage of such a transformation is that the mesh distribution is least restricted and can be controlled easily. The disadvantages are that it leads to considerably more complicated transformed equations, so that the computations are more expensive, and that it may cause larger truncation errors at boundaries where one-sided difference expressions are needed.[10] Hauser *et al.*[5] have employed a non-orthogonal transformation in the numerical study of the shallow water equations. Their scheme became unstable when applied to a practical engineering problem. Stability problems were also encountered in Borthwick and Barber's[9] non-orthogonal model when severe mesh distortion prevailed and a digital smoothing filter was used to treat these instabilities.

Orthogonal co-ordinate systems produce fewer additional terms in the transformed partial differential equations and yet they still allow considerable control over the line spacing. Willemse *et al.*[6] have developed a hydrodynamic model based on an orthogonal transformation, the orthogonal curvilinear grid generated by solving Poisson's equation.

Conformal mapping is a special type of orthogonal transformation. It has the advantage that the governing partial differential equations acquire a minimum number of extra terms on transformation, so that the solution procedures developed for Cartesian co-ordinates may be applicable with only minor changes. Conformal mapping has a very strong theoretical background in complex function theory and many of the results of analytic function theory are useful in the mesh generation process. However, conformal mapping does not provide much control over the grid line distribution. Nevertheless, a more flexible and still orthogonal grid can be generated by augmenting the conformal mapping with simple one-dimensional stretching transformations.

The numerical model DIVAST (Depth-Integrated Velocities And Solute Transport), developed by Falconer,[2,11] is a robust and reliable numerical model for solving the 2D depth-integrated shallow water equations using a uniform rectangular mesh grid. It has been widely used by many U.K. and overseas consultants, universities and research organizations for both industrial and research projects.

In this paper, details are given of the development and application of a 2D depth-integrated finite difference estuarine and coastal model with a conformal boundary-fitted curvilinear mesh. A novel method of numerical conformal mapping, based upon a boundary integral equation formulation, has been used to generate the mesh. The method is able to map a general polygonal region with $2N$ curved sides onto a regular region with the same number of sides: thus it is able to generate curvilinear meshes directly on general curved polygonal regions. If more control over the distribution of the grid mesh lines is necessary, a stretching transformation is then employed. The mesh thus generated is still orthogonal but no longer conformal.

In Section 2 the method for generating the conformal mesh is discussed. In Section 3 the stretching technique for adjusting the distribution of the mesh lines is presented. Section 4 gives the original governing equations in Cartesian co-ordinates. In Sections 5 and 6 the transformed equations are presented and the finite difference scheme used to solve these equations is derived. Section 7 presents three numerical examples: the first two are practical applications to real estuarine tidal flows and the third is solute transport in a meandering flume. In each case, comparisons with field or laboratory data are presented.

2. CONFORMAL MESH GENERATION

To illustrate the idea, we start with the problem of mapping an arbitrary quadrilateral onto a rectangle; see Figure 1. From complex function theory[12] we know that the quadrilateral $\{Q\colon \mathrm{A, B, C, D}\}$ is conformally equivalent to the rectangle $\{\Omega\colon \mathrm{a, b, c, d}\}$, if the ratio L/m is equal to $m(Q)$, the conformal module of $\{Q\colon \mathrm{A, B, C, D}\}$. If $F = u + iv$ is the mapping function $F\colon Q \rightarrow \Omega$, then u and v satisfy the Laplace equations

$$\Delta u = \frac{\partial^2 u}{\partial x^2} + \frac{\partial^2 u}{\partial y^2} = 0, \tag{1a}$$

$$\Delta v = \frac{\partial^2 v}{\partial x^2} + \frac{\partial^2 v}{\partial y^2} = 0 \tag{1b}$$

inside Q and the Cauchy–Riemann equations

$$\frac{\partial u}{\partial s} = \frac{\partial v}{\partial n}, \qquad \frac{\partial u}{\partial n} = -\frac{\partial v}{\partial s} \tag{2}$$

on the boundaries, where $\partial/\partial s$ and $\partial/\partial n$ denote the tangential and normal derivatives respectively, s directed counter-clockwise around ∂Q and n directed into Q. Thus u and v satisfy the boundary value problems shown in Figure 2, in which the subscript n denotes the normal derivative $\partial/\partial n$.

A number of numerical methods have been developed to map the quadrilateral Q onto a rectangle, including finite difference methods, finite element methods and methods based on approximating the conformal mapping of Q onto the unit disc. Most of these methods need iteration to find the conformal module. A survey of the methods can be found in Reference 13.

In the following an alternative method will be presented in which both the conformal module $m(Q)$ and the conformal mapping can be calculated with no iteration.

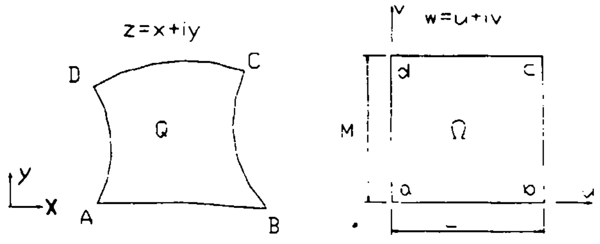

(a) a general quadrilateral (b) a rectangle

Figure 1. Mapping a quadrilateral onto a rectangle

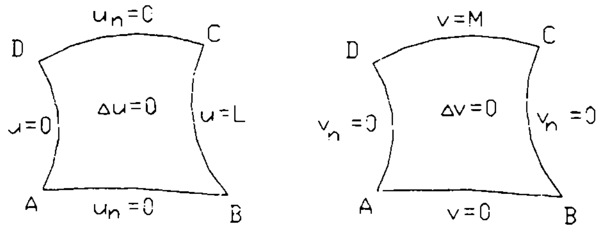

(a) for u = Re(F) (b) for v = Im(F)

Figure 2. Laplace equations and boundary conditions for u and v

From equation (2) the following equations can be obtained:

$$L = -\int_{\mathrm{C}}^{\mathrm{D}} \frac{\partial u}{\partial s} \mathrm{d}s = -\int_{\mathrm{C}}^{\mathrm{D}} \frac{\partial v}{\partial n} \mathrm{d}s, \tag{3a}$$

$$M = \int_{\mathrm{B}}^{\mathrm{C}} \frac{\partial v}{\partial s} \mathrm{d}s = -\int_{\mathrm{B}}^{\mathrm{C}} \frac{\partial u}{\partial n} \mathrm{d}s. \tag{3b}$$

Let u_1 be the solution to the boundary value problem shown in Figure 2(a) with $L = 1$ and let v_1 be the solution to the boundary value problem shown in Figure 2(b) with $M = 1$. We have

$$u = Lu_1, \qquad v = Mv_1. \tag{4}$$

Substituting from equation (4) into equation (3) yields

$$L = -M \int_{\mathrm{C}}^{\mathrm{D}} \frac{\partial v_1}{\partial n} \mathrm{d}s, \tag{5a}$$

$$M = -L \int_{\mathrm{B}}^{\mathrm{C}} \frac{\partial u_1}{\partial n} \mathrm{d}s. \tag{5b}$$

Equations (5) can be written in matrix form as

$$\mathbf{AX} = 0, \tag{6}$$

with

$$\mathbf{A} = \begin{bmatrix} 1 & \displaystyle\int_{\mathrm{C}}^{\mathrm{D}} \frac{\partial v_1}{\partial n} \mathrm{d}s \\ \displaystyle\int_{\mathrm{B}}^{\mathrm{C}} \frac{\partial u_1}{\partial n} \mathrm{d}s & 1 \end{bmatrix}, \qquad \mathbf{X} = \begin{bmatrix} L \\ M \end{bmatrix}.$$

It can be shown that

$$\int_{\mathrm{C}}^{\mathrm{D}} \frac{\partial v_1}{\partial n} \mathrm{d}s \cdot \int_{\mathrm{B}}^{\mathrm{C}} \frac{\partial u_1}{\partial n} \mathrm{d}s - 1 = 0. \tag{7}$$

Thus the rank of the matrix **A** is one and equation (6) has non-trivial solutions. The solution **X** will not be unique, but the ratio $m = L/M$ will be a constant, which is the conformal module of the quadrilateral $\{Q\colon \mathrm{A}, \mathrm{B}, \mathrm{C}, \mathrm{D}\}$.

To compute the map F on the boundary, the following procedure has been employed.

1. Solve the boundary value problems for u_1 and v_1 using the boundary element method[14] on the boundary of the physical domain Q. The boundary element method yields approximations to u_1 and v_1 and their normal derivatives on the boundary of Q.
2. Solve equation (6) together with the condition $L = C$, where C is a constant, approximating the integrals in the matrix **A** by numerical quadrature.
3. Compute $F = u + \mathrm{i}v$ on the boundary using equation (4).

Since $F\colon Q \to \Omega$ is a one-to-one mapping, once the functions $u(x, y)$ and $v(x, y)$ are known at the boundary of the quadrilateral Q in the z-plane, the inverse functions $x(u, v)$ and $y(u, v)$ are also known at the corresponding points of the boundary of the rectangle Ω in the w-plane. Hence the inverse mapping $G = F^{-1}$ can be computed throughout Ω either by solving the Laplace equations on a regular finite difference grid in the w-plane, using, e.g., the ADI method, or by applying numerical quadrature methods to Cauchy's integral formula,[14] which expresses the inverse mapping explicitly. Evaluation of the inverse mapping G at the mesh points of the regular mesh in the computational region Ω determines the location of the mesh points of the orthogonal mesh in the physical region Q.

Note that the above method is able to determine the conformal module of the quadrilateral $\{Q\colon \mathrm{A}, \mathrm{B}, \mathrm{C}, \mathrm{D}\}$ with no iteration.

The above idea can be extended to curvilinear polygonal and multiply connected regions. Consider a curvilinear polygonal region Q with N sides (N being even), as illustrated in Figure 3(a), and a polygon Ω with n vertical sides and n horizontal sides ($n = N/2$), as illustrated in Figure 3(b). In Figure 3(b) for $m = 2, 4, \ldots, N$ the mth side is the vertical side $U = U_m$ and for $m = 1, 3, \ldots, N-1$ the mth side is the horizontal line $V = V_m$. Assume that there exists a conformal mapping F which maps Q onto Ω with $\mathrm{P}_1, \mathrm{P}_2, \mathrm{P}_3, \ldots, \mathrm{P}_N$ being mapped onto $\mathrm{p}_1, \mathrm{p}_2, \mathrm{p}_3, \ldots, \mathrm{p}_N$ respectively. Then $F = u + \mathrm{i}v$, where (cf. Figure 2) u and v satisfy the boundary value problems shown in Figure 4. For $i = 1, 2, \ldots, n$ let $U^{(2i)}$ be the solution of the boundary value problem in Figure 4(a) when $U_{2m} - \delta_{im}$, $m = 1, 2, \ldots, n$ (δ_{im} is the Kronecker delta), and let $V^{(2i-1)}$ be the solution of the boundary value problem in Figure 4(b) when $V_{2m-1} = \delta_{im}$, $m = 1, 2, \ldots, n$. Then

$$U = \sum_{m=1}^{n} U_{2m} U^{(2m)}, \qquad V = \sum_{m=1}^{n} V_{2m-1} V^{(2m-1)}.$$

As described earlier for the case of mapping onto a rectangle, $U^{(2m)}$ and $V^{(2m-1)}$ for $m = 1, 2, \ldots, n$ are determined using the boundary element method. The constants U_{2m} and V_{2m-1} for $m = 1, 2, \ldots, n$ satisfy the following system of equations which generalizes (6):

$$\mathbf{MX} = \mathbf{0}, \tag{8}$$

with

$$\mathbf{M} = \begin{bmatrix} \mathbf{A} & \mathbf{B} \\ \mathbf{C} & \mathbf{D} \end{bmatrix}, \qquad \mathbf{X} = \begin{bmatrix} \mathbf{V} \\ \mathbf{U} \end{bmatrix},$$

where

$$\mathbf{U} = \{U_2, U_4, \ldots, U_N\}^{\mathrm{T}}, \qquad \mathbf{V} = \{V_1, V_3, \ldots, V_{N-1}\}^{\mathrm{T}},$$

$$\mathbf{A} = \begin{bmatrix} -1 & 1 & & \\ & \cdots & & \\ & & -1 & 1 \\ 1 & & & -1 \end{bmatrix}_{n\times n}, \qquad \mathbf{B} = \begin{bmatrix} b_2^2 & b_2^4 & \cdots & b_2^N \\ b_4^2 & b_4^4 & \cdots & b_4^N \\ & & \cdots & \\ b_N^2 & b_N^4 & \cdots & b_N^N \end{bmatrix}_{n\times n},$$

$$\mathbf{C} = \begin{bmatrix} c_1^1 & c_1^3 & \cdots & c_1^{N-1} \\ c_3^1 & c_3^3 & \cdots & c_3^{N-1} \\ & & \cdots & \\ c_{N-1}^1 & c_{N-1}^3 & \cdots & c_{N-1}^{N-1} \end{bmatrix}_{n\times n}, \qquad \mathbf{D} = \begin{bmatrix} -1 & & & 1 \\ 1 & -1 & & \\ & & \cdots & \\ & & 1 & -1 \end{bmatrix}_{n\times n},$$

$$b_l^k = \int_{\Gamma_l} \frac{\partial U^{(k)}}{\partial n}\,\mathrm{d}s, \quad l = 2, 4, \ldots, N, \quad k = 2, 4, \ldots, N,$$

$$c_l^k = \int_{\Gamma_l} \frac{\partial V^{(k)}}{\partial n}\,\mathrm{d}s, \quad l = 1, 3, \ldots, N-1, \quad k = 1, 3, \ldots, N-1.$$

The vector of unknowns **X** is determined by solving, using a least squares method, equation (8) together with the additional constraints $V_1 = 0$, $U_2 = 0$ and $V_{N-1} = C$ for some constant C, which fix the position and size of Ω. For further details and the extensions to the multiply connected case see Reference 19.

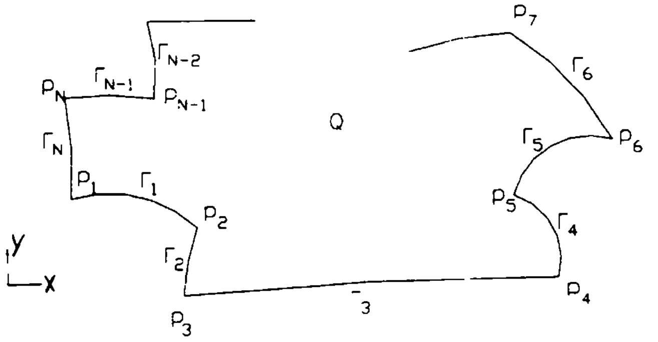

(a) a curvilinear polygonal region

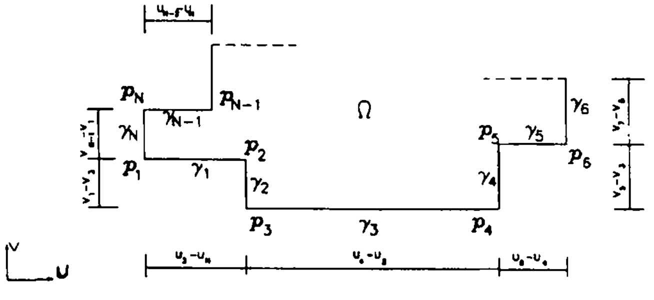

(b) a rectilinear region

Figure 3. Mapping a curvilinear polygonal region onto a rectilinear region

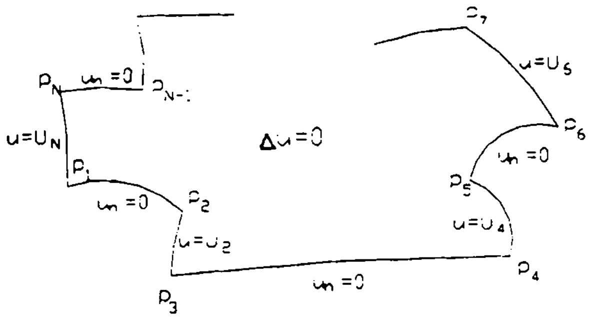

(a) for u = Re(F)

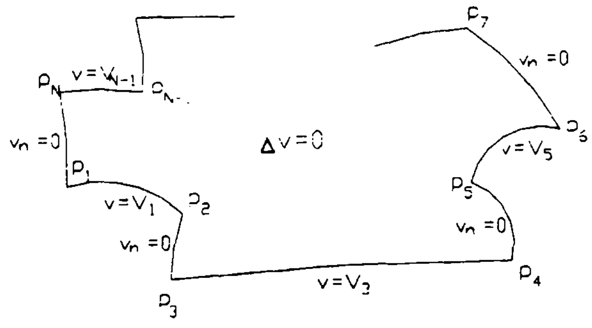

(b) for v = Im(F)

Figure 4. Laplace equations and boundary conditions for *u* and *v*

3. LOCAL MESH LINE REDISTRIBUTION

The advantage of using a co-ordinate system generated by conformal mapping is that the number of extra terms caused by transforming the governing equation from Cartesian co-ordinates to curvilinear co-ordinates is minimized. However, this mapping does not have much control over the grid point distribution in the physical domain, since the conformal mapping is uniquely determined once the positions of the points $P_1, P_2, P_3, \ldots, P_N$ on the physical boundary are decided. Therefore, if a fine mesh is required in some particular regions of interest, e.g. near an outfall, the mesh for the whole domain must also be increased.

One way to increase the flexibility of mesh size control is to redistribute the conformally generated mesh by introducing a stretching transformation. It is clear[16] that one-dimensional stretching transformations applied to a conformally generated mesh can maintain the orthogonality of the original mesh but not the conformality. In this way the mesh resolution can be increased in key regions with only a moderate increase in computational cost.

To describe the modified mesh generation procedure, we introduce the one- dimensional stretching transformations k_1 and k_2, both real-valued functions of a single real variable and strictly monotonic increasing. The modified procedure is as follows.

1. Set up a rectangular grid in the ξ–η plane.
2. Transform this to a stretched rectangular grid in the u–v plane, point (ξ, η) mapped to (u, v) with $u = k_1^{-1}(\xi)$ and $v = k_2^{-1}(\eta)$.

3. Transform the stretched rectangular grid conformally onto the physical region, the point $w = u + iv$ mapped onto $z = x + iy = G(w)$, where G is the conformal mapping calculated as described in the previous section.

4. GOVERNING EQUATIONS IN THE CARTESIAN CO-ORDINATE SYSTEM

The mathematical model used in this study, in Cartesian co-ordinates, can be described by the following depth-integrated two-dimensional momentum, mass conservation and solute transport equations. For a constant density turbulent flow on a rotating earth the depth-integrated momentum equations for flow in the horizontal co-ordinate directions x and y can be expressed respectively as[17]

$$\underset{1}{\frac{\partial q_x}{\partial t}} + \underset{2}{\beta\left(\frac{\partial}{\partial x}(U_x q_x) + \frac{\partial}{\partial y}(U_x q_y)\right)} \underset{3}{- f q_y} + \underset{4}{gH\frac{\partial \zeta}{\partial x}} - \underset{5}{\frac{\rho_a}{\rho} C^* W_x W} + \underset{6}{g\frac{U_x U}{Cz^2}} - \underset{7}{\varepsilon H\left(\frac{\partial^2 U_x}{\partial x^2} + \frac{\partial^2 U_x}{\partial y^2}\right)} = 0, \tag{9}$$

$$\frac{\partial q_y}{\partial t} + \beta\left(\frac{\partial}{\partial x}(U_y q_x) + \frac{\partial}{\partial y}(U_y q_y)\right) + f q_x + gH\frac{\partial \zeta}{\partial y} - \frac{\rho_a}{\rho} C^* W_y W + g\frac{U_y U}{Cz^2} - \varepsilon H\left(\frac{\partial^2 U_y}{\partial x^2} + \frac{\partial^2 U_y}{\partial y^2}\right) = 0, \tag{10}$$

where H is the depth of flow, U_x and U_y are the depth-mean velocity components in directions x and y respectively, $U = (U_x^2 + U_y^2)^{1/2}$, $q_x = U_x H$, $q_y = U_y H$, t is the time, β is a correction factor for non-uniformity of the vertical velocity profile ($= 1{\cdot}016$ for assumed seventh-power-law profile), f is the Coriolis parameter, g is the acceleration due to gravity, ζ is the water elevation, ρ_a is the air density, ρ is the fluid density, C^* is the air–water interfacial resistance coefficient, W_x and W_y are the components of wind velocity in the directions x and y respectively. $W = (W_x^2 + W_y^2)^{1/2}$, Cz is the Chezy bed roughness coefficient and ε is the depth mean eddy viscosity. In equation (9) the various terms are the depth-integral local acceleration (term 1), advective acceleration (term 2), Coriolis force (term 3), pressure gradient (term 4), wind shear force (term 5), bed shear resistance (term 6) and turbulence-induced shear force (term 7).

The Chezy value Cz can be evaluated either from the Manning equation or from the Colebrook–White equation. The advantage of using the Colebrook–White equation to calculate Cz is that the value of the roughness coefficient k_S can be more closely related to bed features, such as ripples or dunes, and the representation of the Chezy value can include transitional turbulent flow. This refinement can be particularly important when modelling the flooding and drying processes of tidal flood plains, where Reynolds number effects may not be insignificant.[18] The lateral shear stress is represented by the Boussinesq eddy viscosity, and with a zero-equation turbulence model.

Likewise, the depth-integrated conservation equations of mass and solute transport can be written respectively as

$$\frac{\partial \zeta}{\partial t} + \frac{\partial q_x}{\partial x} + \frac{\partial q_y}{\partial y} = 0, \tag{11}$$

$$\begin{aligned} &\frac{\partial (CH)}{\partial t} + \frac{\partial (Cq_x)}{\partial x} + \frac{\partial (Cq_y)}{\partial y} - \frac{\partial}{\partial x}\left(HD_{xx}\frac{\partial C}{\partial x} + HD_{xy}\frac{\partial C}{\partial y}\right) \\ &\quad - \frac{\partial}{\partial y}\left(HD_{yx}\frac{\partial C}{\partial x} + HD_{yy}\frac{\partial C}{\partial y}\right) - H(C_L + C_B + C_k) = 0, \end{aligned} \tag{12}$$

where C is the depth-mean solute concentration, D_{xx}, D_{xy}, D_{yx} and D_{yy} are the mean dispersion coefficients in the directions x and y respectively, C_L is the direct and diffuse loading rate, C_B is the boundary loading rate (including upstream, downstream, benthic and atmospheric inputs) and C_k is the total kinetic transformation rate.

5. TRANSFORMED GOVERNING EQUATIONS

In the orthogonal co-ordinate system, equations (9)–(12) can be written as follows:
ξ-momentum

$$\underset{1}{\frac{\partial q_\xi}{\partial t}} + \beta\left[\underset{2a}{\frac{1}{J}\left(\frac{\partial}{\partial \xi}(U_\xi h_2 q_\xi) + \frac{\partial}{\partial \eta}(U_\xi h_1 q_\eta)\right)} + \underset{2b}{\frac{U_\eta}{J}\left(q_\xi \frac{\partial h_1}{\partial \eta} - q_\eta \frac{\partial h_2}{\partial \xi}\right)}\right] \underset{3}{-fq_\eta} + \underset{4}{\frac{gH}{h_1}\frac{\partial \zeta}{\partial \xi}}$$

$$\underset{5}{-\frac{\rho_a}{\rho}C^* W_\xi W} + \underset{6}{g\frac{U_\xi U}{Cz^2}} - \varepsilon H\left[\underset{7a}{\frac{1}{h_1}\frac{\partial}{\partial \xi}\left(\frac{1}{J}\frac{\partial}{\partial \xi}(h_2 U_\xi)\right) + \frac{1}{h_2}\frac{\partial}{\partial \eta}\left(\frac{1}{J}\frac{\partial}{\partial \eta}(h_1 U_\xi)\right)}\right.$$

$$\left.\underset{7b}{\frac{1}{h_1}\frac{\partial}{\partial \xi}\left(\frac{1}{J}\frac{\partial}{\partial \eta}(h_1 U_\eta)\right) - \frac{1}{h_2}\frac{\partial}{\partial \eta}\left(\frac{1}{J}\frac{\partial}{\partial \xi}(h_2 U_\eta)\right)}\right] = 0, \tag{13}$$

η-momentum

$$\frac{\partial q_n}{\partial t} + \beta\left[\frac{1}{J}\left(\frac{\partial}{\partial \xi}(U_\eta h_2 q_\xi) + \frac{\partial}{\partial \eta}(U_\eta h_1 q_\eta)\right) + \frac{U_\xi}{J}\left(q_\eta \frac{\partial h_2}{\partial \xi} - q_\xi \frac{\partial h_1}{\partial \eta}\right)\right] + fq_\xi + \frac{gH}{h_2}\frac{\partial \zeta}{\partial \eta}$$

$$-\frac{\rho_a}{\rho}C^* W_\eta W + g\frac{U_\eta U}{C_z^2} - \varepsilon H\left[\frac{1}{h_1}\frac{\partial}{\partial \xi}\left(\frac{1}{J}\frac{\partial}{\partial \xi}(h_2 U_\eta)\right) + \frac{1}{h_2}\frac{\partial}{\partial \eta}\left(\frac{1}{J}\frac{\partial}{\partial \eta}(h_1 U_\eta)\right)\right.$$

$$\left.\frac{1}{h_2}\frac{\partial}{\partial \xi}\left(\frac{1}{J}\frac{\partial}{\partial \xi}(h_2 U_\xi)\right) - \frac{1}{h_1}\frac{\partial}{\partial \eta}(h_2 U_\xi)\right)\right] = 0, \tag{14}$$

mass conservation

$$\frac{\partial \zeta}{\partial t} + \frac{1}{J}\left(\frac{\partial (h_2 q_\xi)}{\partial \xi} + \frac{\partial (h_1 q_\eta)}{\partial \eta}\right) = 0, \tag{15}$$

solute conservation

$$\frac{\partial (CH)}{\partial t} + \frac{1}{h_1 h_2}\left(\frac{\partial}{\partial \xi}(h_2 C q_\xi) + \frac{\partial}{\partial \eta}(h_1 C q_\eta)\right) - \frac{1}{h_1 h_2}\left[\frac{\partial}{\partial \xi}\left(HD_{11}\frac{\partial C}{\partial \xi}\right) + \frac{\partial}{\partial \xi}\left(HD_{12}\frac{h_1 \partial C}{h_2 \partial \eta}\right)\right]$$

$$-\frac{1}{h_1 h_2}\left[\frac{\partial}{\partial \eta}\left(HD_{21}\frac{h_2 \partial C}{h_1 \partial \xi}\right) + \frac{\partial}{\partial \eta}\left(HD_{12}\frac{\partial C}{\partial \eta}\right)\right] = H(C_L + C_B + C_k), \tag{16}$$

where h_1 and h_2 are the transformation scale factors in the directions ξ and η respectively, $J = h_1 h_2$ and the subscripts ξ and η denote the vector components in the directions ξ and η respectively. Note that, adopting the mesh generation scheme of Section 3, explicitly, $h_1 = |G'(w)|/k_1'(u)$ and $h_2 = |G'(w)|/k_2'(v)$, where $u = k_1^{-1}(\xi)$, $v = k_2^{-1}(\eta)$ and $w = u + iv$.

In equation (13) the numbering of terms corresponds to that in equation (9). Comparing equation (13) with (9), it can be seen that terms 1, 2a, 3, 4, 5, 6, and 7a in (13) are, apart from the introduction of the scale factors h_1 and h_2, identical with terms 1–7 in (9). The additional terms 2b and 7b are associated with the spatial rate of change of the scale factors (see also Reference 19).

If the transformation used is conformal, (e.g. if the scheme of Section 2 is used), equations (13)–(16) can be simplified further using the Cauchy–Riemann equations (2), since it is then the case that $h_1 = h_2$.

6. NUMERICAL SCHEME

6.1. The hydrodynamic model

A finite difference discretization of the hydrodynamic equations (9)–(11) written in an alternating direction implicit form using a space-staggered grid scheme was presented in Reference 17. This discretization has been modified to obtain finite difference versions of the transformed equations (13)–(15). In developing and applying this curvilinear co-ordinate model, emphasis has been focused on modelling the complex hydrodynamic processes in practical engineering problems. For example, to simulate flooding and drying, the scheme outlined by Falconer and Chen[20] was modified for use on the curvilinear grid.

In order that the geometric derivatives can be specified at the cell centres and mid-faces, following Borthwick and Barber,[9] the co-ordinate mesh for the required flow domain is generated with twice as many cells in each direction as are required for the final hydrodynamic mesh.

For the first half-time step from level n to $n + \frac{1}{2}$ the mass conservation equation (15) is discretized and rearranged to give

$$-r_{j-1/2}(q_\xi)^{n+1/2}_{j-1/2,k} + \zeta^{n+1/2}_{j,k} + r_{j+1/2}(q_\xi)^{n+1/2}_{j+1/2,k} = A^{n-1/2}_{j,k}, \tag{17}$$

where

$$r_{j-1/2} = \frac{\Delta t}{2J_{j,k}}\frac{(h_2)_{j-1/2,k}}{\Delta\xi}, \qquad r_{j+1/2} = \frac{\Delta t}{2J_{j,k}}\frac{(h_2)_{j+1/2,k}}{\Delta\xi},$$

$$A^{n-1/2}_{j,k} = \zeta^n_{j,k} - \frac{\Delta t}{2J_{j,k}}\frac{1}{\Delta\eta}[(h_1 q_\eta)^n_{j,k+1/2} - (h_1 q_\eta)^n_{j,k-1/2}].$$

The subscripts j and k denote a value at the grid point with co-ordinates $\xi = j\Delta\xi$ and $\eta = k\Delta\eta$ and the superscript n indicates time $t = n\Delta t$. The ξ-direction momentum equation (13) is discretized and rearranged to give

$$-s_j\zeta^{n+1/2}_{j,k} + s_{j+1/2}(q_\xi)^{n+1/2}_{j+1/2} + s_{j+1}\zeta^{n+1/2}_{j,k} = B^{n-1/2}_{j+1/2,k}, \tag{18}$$

where

$$s_{j+1} = s_j = g\frac{\Delta t}{2\Delta\xi}\left(\frac{H}{h_1}\right)^n_{j+1/2,k}, \qquad s_{j+1/2} = 1 + \Delta t g\left(\frac{U}{2HCz^2}\right)^n_{j+1/2,k},$$

$$\begin{aligned} B^{n-1/2}_{j+1/2,k} = (q_\xi)^n_{j+1/2,k} - \frac{\beta\Delta t}{J_{j+1/2,k}}\Bigg[\Bigg(&\frac{1}{\Delta\xi}[(h_2U'_\xi q'_\xi)^n_{j+1,k} - (h_2U'_\xi q'_\xi)^n_{j,k}] \\ &+ \frac{1}{\Delta\eta}[(h_1q_\eta)^n_{j+1/2,k+1/2}(U'_\xi)^n_{j+1/2,k+p} - (h_1q_\eta)^n_{j+1/2,k-1/2}(U'_\xi)^n_{j+1/2,k-1+q}]\Bigg) \\ &+ (U_\eta)^n_{j+1/2,k}\Bigg((q'_\xi)^n_{j+1/2,\,j+1/2,k}\frac{1}{\Delta\eta}[(h_1)_{j+1/2,k+1/2} - (h_1)_{j+1/2,k-1/2}] \\ &- (q_\eta)^n_{j+1/2,\,j+1/2,k}\frac{1}{\Delta\xi}[(h_2)_{j+1,k} - (h_2)_{j,k}]\Bigg) \end{aligned}$$

$$
\begin{aligned}
&+\Delta t f(q\eta)^{n}_{j+1/2}-g\frac{\Delta t}{2\Delta\xi}\left(\frac{H}{h_1}\right)^{n}_{j+1/2,k}(\zeta^{n-1/2}_{j+1,k}-\zeta^{n-1/2}_{j,k})+\Delta t\frac{\rho_{\mathrm{a}}}{\rho}W_\xi W\\
&-g\Delta t\left(\frac{U}{2HCz^2}\right)^{n}_{j+1/2,k}(q_\xi)^{n-1/2}_{j+1/2,k}\\
&+\Delta t(\varepsilon H)^{n}_{j+1/2,k}\left[\frac{1}{(h_1)_{j+1/2,k}}\frac{1}{\Delta\xi^2}\left(\frac{1}{J_{j+1,k}}[(h_2U'_\xi)^{n}_{j+1/2,k}-(h_2U'_\xi)^{n}_{j+1/2,k}]\right.\right.\\
&\left.-\frac{1}{J_{j,k}}[(h_2U'_\xi)^{n}_{j+1/2,k}-(h_2U'_\xi)^{n}_{j-1/2,k}]\right)\\
&+\frac{1}{(h_2)_{j+1/2,k}}\frac{1}{\Delta\eta^2}\left(\frac{1}{J_{j+1/2,k+1/2}}[(h_1U'_\xi)^{n}_{j+1/2,k+1}-(h_1U'_\xi)^{n}_{j+1/2,k}]\right.\\
&\left.-\frac{1}{J_{j+1/2,k-1/2}}[(h_1U'_\xi)^{n}_{j+3/2,k}-(h_1U'_\xi)^{n}_{j+3/2,k-1}]\right)\\
&+\frac{1}{(h_1)_{j+1/2,k}}\frac{1}{\Delta\xi\Delta\eta}\left(\frac{1}{J_{j+1,k}}[(h_1U_\eta)^{n}_{j+1,k+1/2}-(h_1U_\eta)^{n}_{j+1,k-1/2}]\right.\\
&\left.-\frac{1}{J_{j,k}}[(h_1U_\eta)^{n}_{j,k+1/2}-(h_1U_\eta)^{n}_{j,k-1/2}]\right)\\
&-\frac{1}{(h_2)_{j+1/2,k}}\left(\frac{1}{J_{j+1,2,k}}[(h_2U_\eta)^{n}_{j+1,k+1/2}-(h_2U_\eta)^{n}_{j,k+1/2}]\right.\\
&\left.\left.-\frac{1}{J_{j+1/2,k-1/2}}[(h_2U_\eta)^{n}_{j+1,k-1/2}-(h_2U_\eta)^{n}_{j,k-1/2}]\right)\right].
\end{aligned}
$$

In this equation,

$$P=\begin{cases}1 & \text{if} \quad U^{*}_{\eta}<0,\\ 0 & \text{if} \quad U^{*}_{\eta}>0,\end{cases}$$

where

$$U^{*}_{\eta}=\tfrac{1}{4}\left[(U_\eta)^{n}_{j,k+1/2}+(U_\eta)^{n}_{j,k-1/2}+(U_\eta)^{n}_{j+1,k+1/2}+(U_\eta)^{n}_{j+1,k-1/2}\right],$$

and q is determined similarly. Equations (17) and (18) are used iteratively in a two-stage predictor–corrector mode. For the first iteration, equations (17) and (18) are solved with the terms written with a prime replaced by the values of the same variables calculated at time step $n-\frac{1}{2}$. At the second iteration these terms are expressed in time-centre form at level n using the mean of the values calculated at the previous time step and at the end of the first iteration.

Similarly, for the second half time-step from level $n+\frac{1}{2}$ to $n+1$, implicit finite difference discretizations of the continuity equation (15) and of the η-component momentum equation (14) are solved for q_η and ζ.

Define the Courant number Cr by

$$Cr=\frac{\Delta t}{\Delta_{\min}}\sqrt{(gH_{\max})}, \tag{19}$$

where $\Delta_{\min} = \min(\sqrt{(h_1 \Delta\xi \cdot h_2 \Delta\eta)})$, the minimum mean mesh diameter over all grid squares. From computations with various test examples it appears that a Courant number of not greater than approximately $Cr = 8$ is necessary for accurate predictions. These observations are also reported for the regular grid scheme of the original method DIVAST, to which this scheme reduces if $h_1 = h_2 = 1$.

The Coriolis acceleration term in equation (18) may cause stability problems as it is approximated forwards in time. Generally speaking, this problem is more pronounced in deeper water than in shallower water. In the present study the water depths encountered are scarcely bigger than 50 m, so the Coriolis effects on stability are small compared with the effects of other terms in equation (18).

The solute transport model

For the finite difference representation of the solute transport equation (16) the ADI version of the QUICK difference scheme was adopted with a semi-implicit representation for the higher-order terms. The QUICK finite difference scheme is based on assuming quadratic upstream interpolation and was first proposed by Leonard[21] for steady flows. This scheme has been increasingly used in recent years for water quality modelling owing to its computational efficiency and simplicity. When the scheme is applied to unsteady flows, several finite difference forms exist. After comparing five versions of the 2D unsteady QUICK scheme, Chen and Falconer[22] found that the semi-implicit version of the QUICK scheme was computationally efficient and almost as accurate as the fully time-centred implicit scheme.

For brevity, only the discretization of the orthogonal form of the advection– diffusion equation (16) will be presented. For the first half-time step from level n to $n + \frac{1}{2}$ the finite difference scheme is expressed in the form

$$\begin{aligned}
(CH)_{j,k}^{n+1/2} - (CH)_{j,k}^{n} + \Bigg(& \frac{1}{\Delta\xi}[(h_2 q_\xi)_{j+1/2,k}^{n+1/2}(C_{j+1,k}^{n+1/2} + C_{j,k}^{n+1/2}) - (h_2 q_\xi)_{j-1/2,k}^{n+1/2}(C_{j,k}^{n+1/2} + C_{j-1,k}^{n+1/2})] \\
& - \frac{1}{\Delta\eta}[(h_1 q_\eta)_{j,k+1/2}^{n}(C_{j,k+1}^{n} + C_{j,k}^{n}) - (h_1 q_\eta)_{j,k-1/2}^{n}(C_{j,k}^{n} + C_{j,k-2}^{n})] \\
& - \frac{1}{4\Delta\xi}[(h_2 q_\xi)_{j+1/2,k}^{n+1/2}\Delta_{11}C_{j+1/2,k}^{n} - (h_2 q_\xi)_{j-1/2,k}^{n+1/2}\Delta_{11}C_{j-1/2,k}^{n}] \\
& - \frac{1}{4\Delta\eta}[(h_1 q_\eta)_{j,k+1/2}^{n}\Delta_{22}C_{j,k+1/2}^{n} - (h_1 q_\eta)_{j,k+1/2}^{n}\Delta_{22}C_{j,k+1/2}^{n}]\Bigg)\frac{\Delta t}{4h_1 h_2} \\
& = \text{dispersion and diffusion} + \text{source or sink} + \text{decay and interaction,}
\end{aligned} \tag{20}$$

where

$$\Delta_{11}C_{j+1/2,k} = \begin{cases} C_{j+1,k} - 2C_{j,k} + C_{j-1,k}, & U_{j+1/2,k} > 0, \\ C_{j-2,k} - 2C_{j+1,k} + C_{j,k}, & U_{j+1/2,k} < 0, \end{cases}$$

and similarly

$$\Delta_{22}C_{j,k+1/2} = \begin{cases} C_{j,k+1} - 2C_{j,k} + C_{j,k-1}, & U_{j,k+1/2} > 0, \\ C_{j,k+2} - 2C_{j,k+1} + C_{j,k}, & U_{j,k+1/2} < 0. \end{cases}$$

The dispersion–diffusion terms are expressed in a fully centred form, as done by Falconer[17] for the Cartesian form of the equation.

7. MODEL VERIFICATION AND APPLICATIONS

Three test cases were used to test the model performance, namely (i) tidal propagation in the Bristol Channel, U.K., (ii) tidal propagation and solute transport in the Humber Estuary, U.K. and (iii) flow and solute transport in a laboratory meandering channel.

Case study 1

The conformal mesh model was applied to simulate tidal elevations and currents in the Bristol Channel. The original, rectilinear finite difference model was also used for comparison purposes. Figure 5 shows the part of the Bristol Channel modelled, together with the approximations to the true boundary adopted in the curvilinear and rectilinear models. The tidal range in the Bristol Channel is one of the highest in the world. Thus accurate modelling of the tidal flow is a very severe test. The region was originally represented by a regular mesh of 81 × 57 grid points with a constant grid spacing of 1800 m. The bathymetry of the basin was represented by prescribing the depth below Chart Datum at the centre of each grid square. These data were obtained from Admiralty Chart No. 1179.

Two boundary-fitted meshes were generated (see Figures 6 and 7) using the conformal method described in Section 2. In generating Figure 6, the physical domain was considered as a quadrilateral and mapped onto a rectangle. As with other elliptic grid generation methods (without control functions), large grid cells tend to appear in regions of strong concave curvature and small grid cells appear in the vicinity of strong convex boundary curvature. Obviously, excessively large or small grid cells existing in the same mesh will cause inaccuracy and be computationally expensive. In generating Figure 7, the physical domain was considered as a curvilinear polygonal region with six sides and so was mapped onto a polygon with six sides. It can be seen that the excessively large and small grid cells have been eliminated.

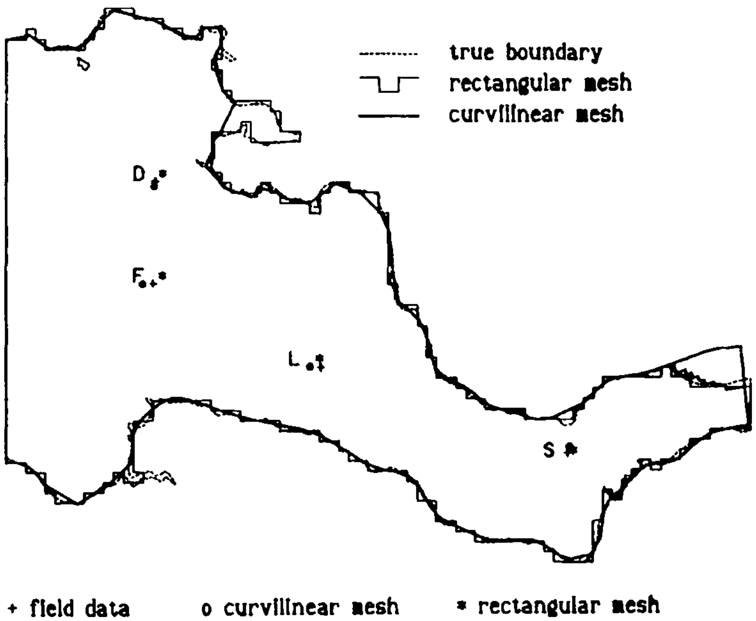

Figure 5. Part of Bristol Channel modelled and approximations to true boundary used in curvilinear and rectilinear models

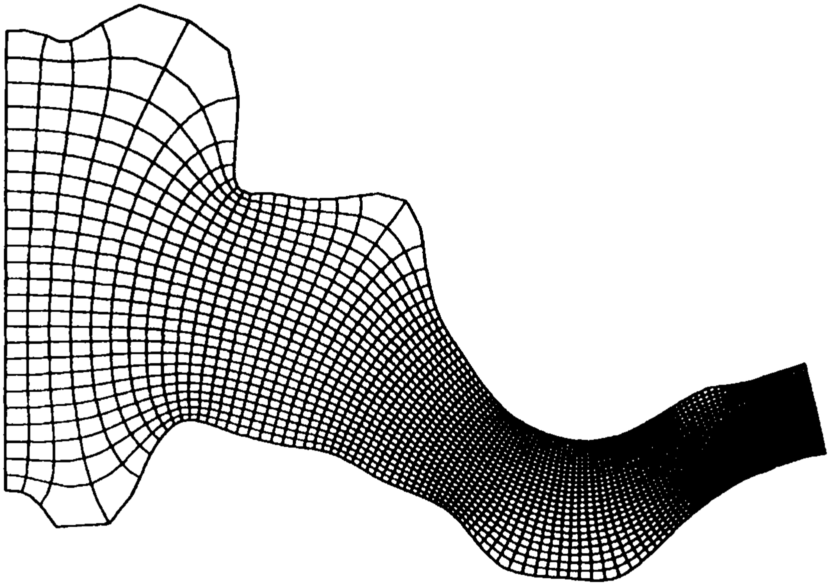

Figure 6. Conformal boundary-fitted mesh for British Channel, generated via conformal mapping onto a rectangle

In the following the mesh shown in Figure 7 was used for the hydrodynamic modelling. The depths for each grid square centre were interpolated from the regular 1800 m square mesh using the method of bilinear interpolation. The simulation period was 62·0 h (five tidal cycles), with the first four tidal cycles being the model warm-up period.

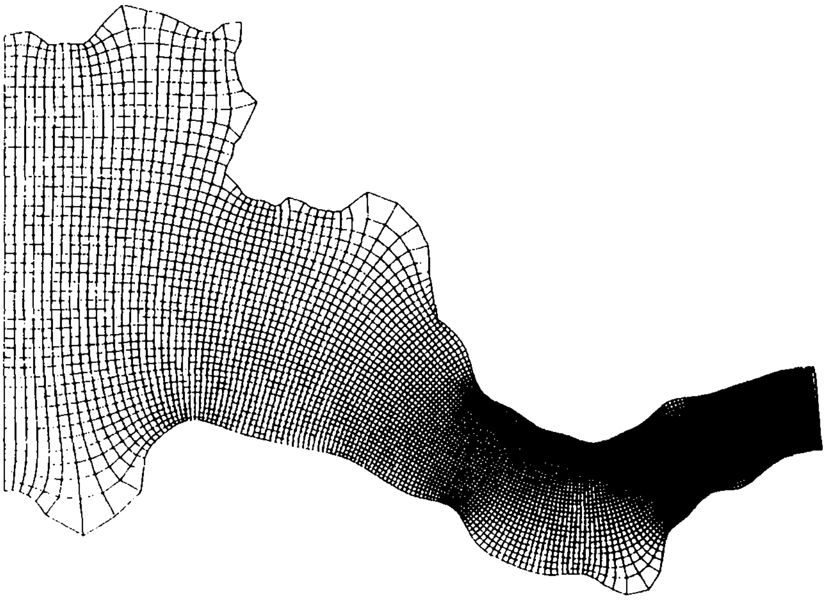

Figure 7. Conformal boundary-fitted mesh for British Channel, generated via conformal mapping onto a six-edged polygon

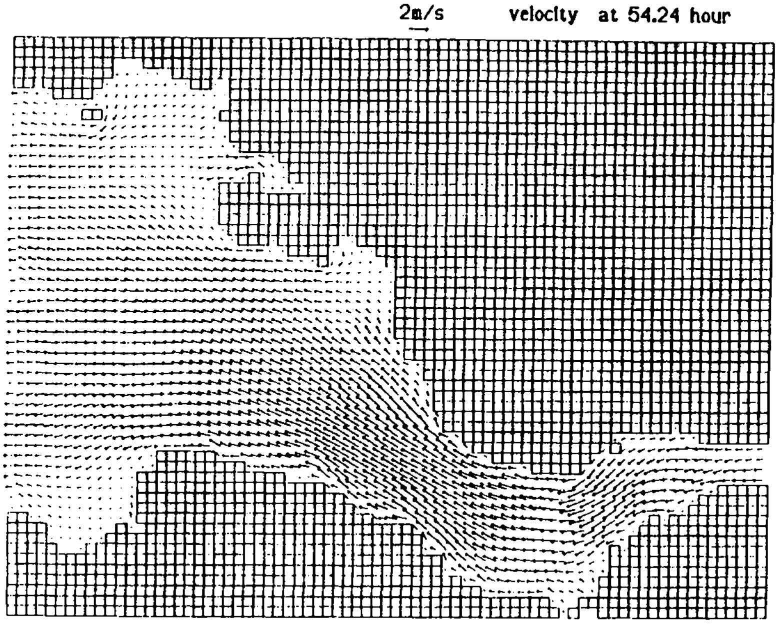

Figure 8. Velocity predictions in Bristol Channel using regular mesh

Figures 8 and 9 show predictions of the velocities at a typical point in the tidal cycle at spring tide for the rectilinear and curvilinear models respectively. The shaded areas represent dry land. Both predictions were driven by the same boundary conditions. A no-slip boundary condition was imposed on the coastline. At the landward open boundary the water elevation was specified from tide tables. At the seaward open boundary the water elevation was specified at the bottom corner from tide tables

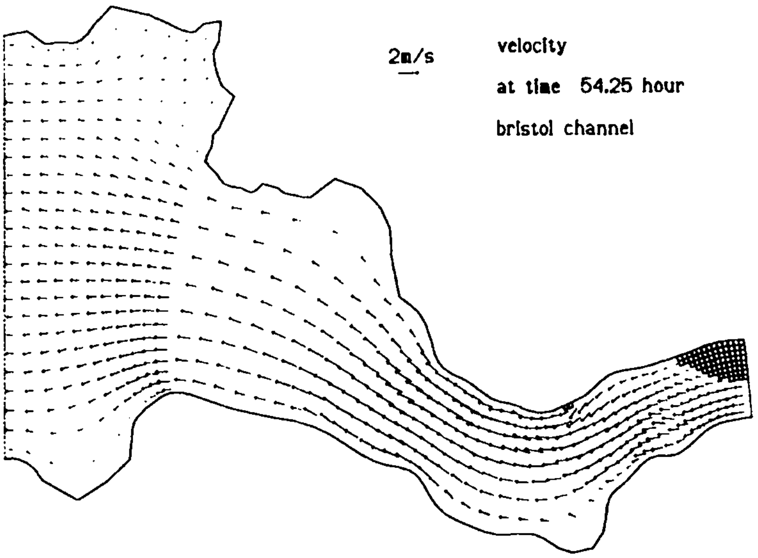

Figure 9. Velocity predictions in Bristol Channel using curvilinear mesh

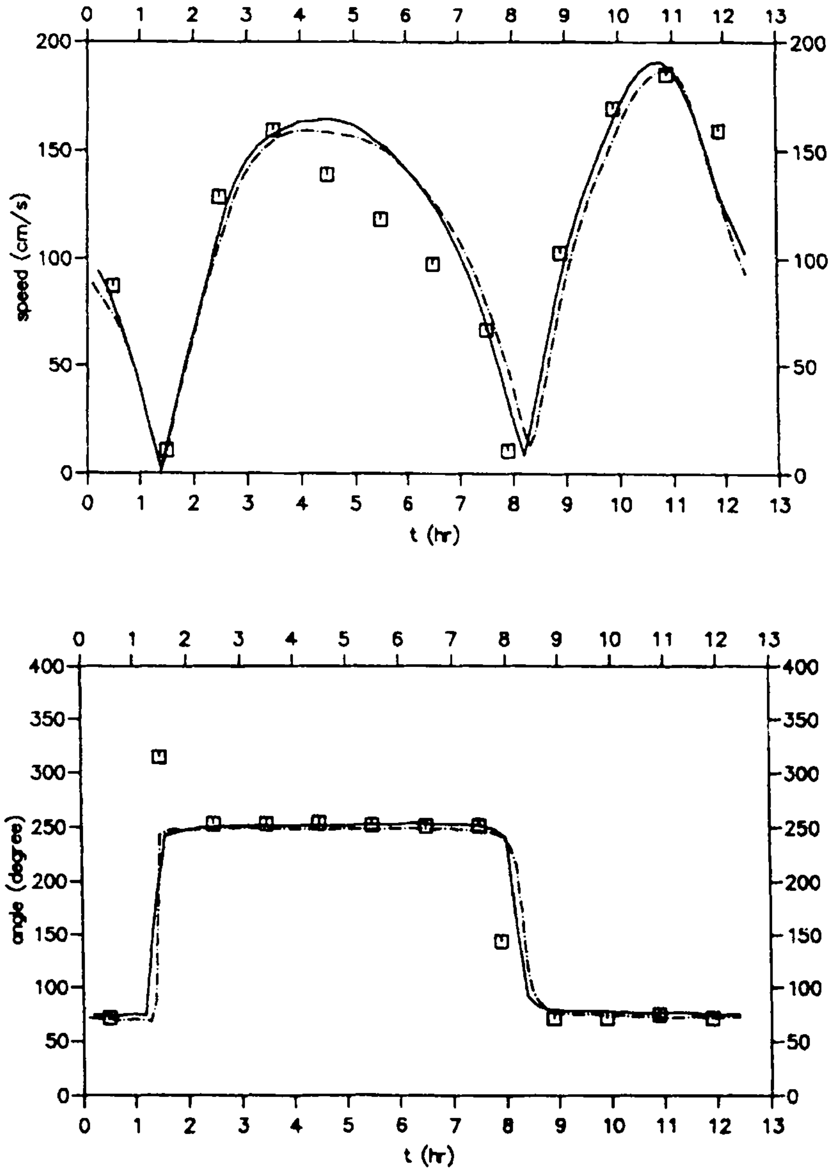

Figure 10. Comparison of velocities between field data (☐) and regular (-----) and curvilinear model (—) predictions at point S in Figure 5

and the water elevation along the boundary was calculated by applying a Coriolis slope given by[17]

$$\frac{\partial \zeta}{h \partial \eta} = f \frac{U_{\xi}}{g}, \tag{21}$$

with U_{η} being set to zero.

Comparing the two predictions, it can be seen that the rectilinear model generally provides a more detailed prediction at the downstream end of the estuary. The curvilinear model represents the flow

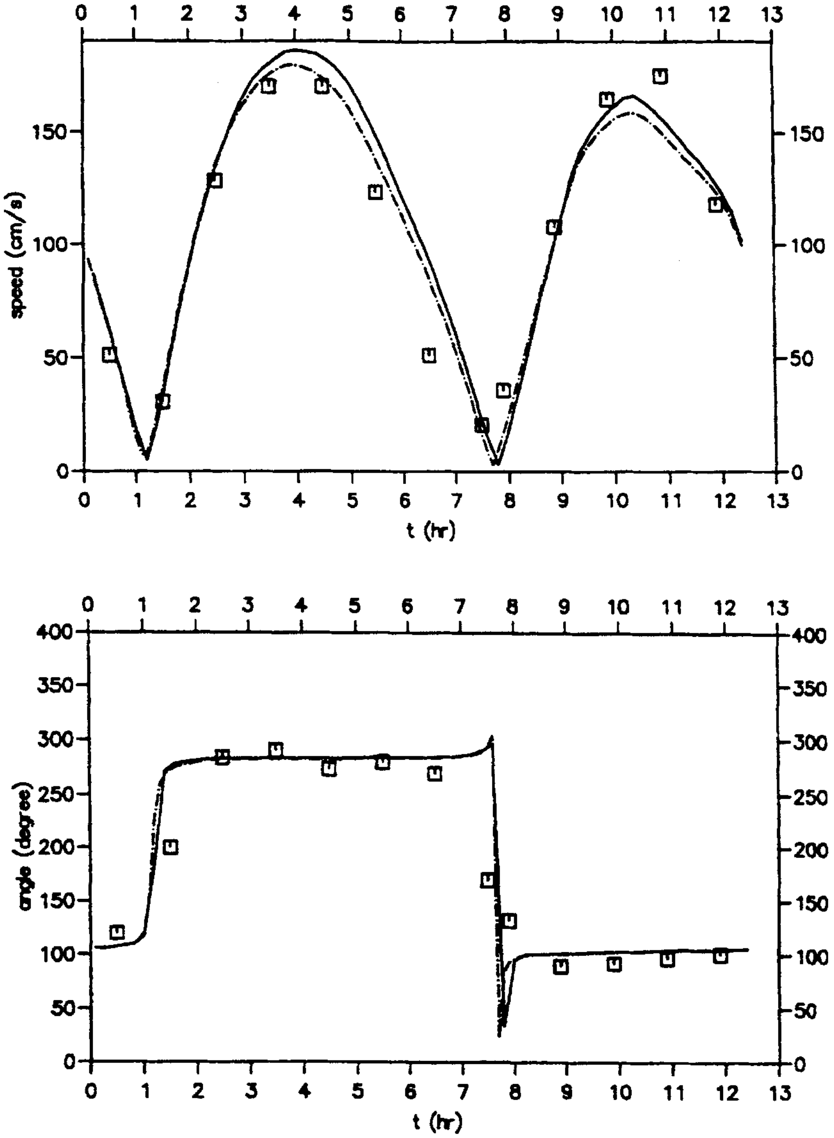

Figure 11. Comparison of velocities between field data (□) and regular (----) and curvilinear model (—) predictions at point L in Figure 5

upstream in more detail, in particular the extensive flooding and drying in this region. Also, it avoids the generation of vorticity at artificial corners of the domain as seen in the regular grid calculations.

Comparisons of flow speed and direction have also been made at four points as shown in Figure 5. Figures 10 and 11 illustrate the comparisons at points S and L respectively. It can be seen that the agreement between the two models is good, with the agreement between both models and the field data also being reasonable. The fit at all other points examined was of a similar quality.

Case study 2

The tidal motion in the Humber Estuary was then chosen as an example to verify the capability of the orthogonal model as well as the conformal model. The Humber Estuary is situated along the north-east coast of England, providing an outlet to the North Sea for the rivers Trent and Ouse and shipping access to a number of ports, including Hull, Immingham and Grimsby (see Figure 12). Data relating to the hydrodynamic conditions in the estuary were supplied by Associated British Ports (formerly British Transport Docks Board).[23,24] In order to test the solute transport model, a pollutant source (outfall) was assumed to exist at a point downstream of Halton Middle, marked by an asterisk in Figure 12.

Owing to the lack of suitable bed roughness data, several authors, including Owens[25] and Cahyono,[26] have previously calibrated the bed roughness for models of the Humber Estuary. Owens used a constant value throughout the whole estuary, while Cahyono employed two constant values for the bed roughness, with the value being determined by the magnitude of the local fluid speed. Owing to the sparseness of the data and the absence of bed shear measurements, a constant bed roughness value seemed most appropriate for the current study. In the following simulations a bed roughness value of 0·02 m (as given by Owens[25]) was therefore used.

To show the merits and restrictions of the conformal mapping and stretching technique, a boundary-fitted mesh was first generated using the conformal mesh generation method. Figure 13(a) shows the original boundary and the boundary-fitted mesh (the shaded squares are dry land). The number of cells is 130 in the ξ-direction, with six in the narrower part and 25 in the wider part in the η-direction. It can be seen that the mesh size near the landward boundary is smaller than that near the seaward boundary. This property is attractive in modelling fluxes along the Humber Estuary, since a constant size square mesh is too coarse for the upper part of the estuary, where the meandering deeper channel is typically less than 500 m wide. Note also that the width of the cells representing the narrow peninsular near Spurn Head is much greater than the actual width.

An orthogonal mesh was then generated (Figure 13(b)) using the stretching technique to get a better representation of the narrow peninsular near Spurn Head and a higher resolution near the outfall site. Compared with the conformal mesh, it can be seen that (i) the narrow peninsular near

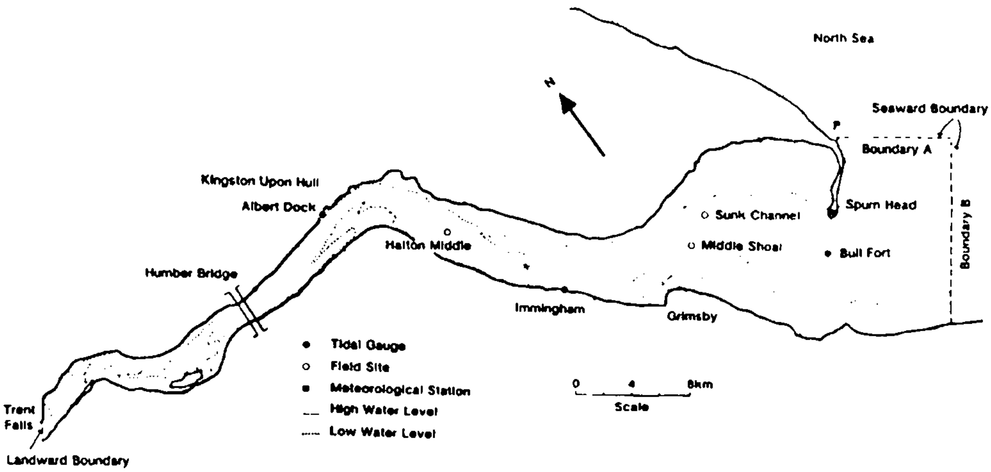

Figure 12. Plan of Humber Estuary

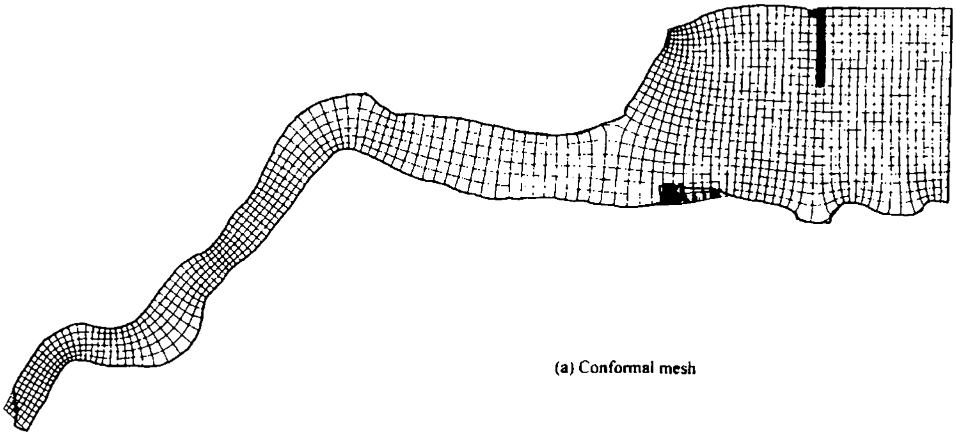

(a) Conformal mesh

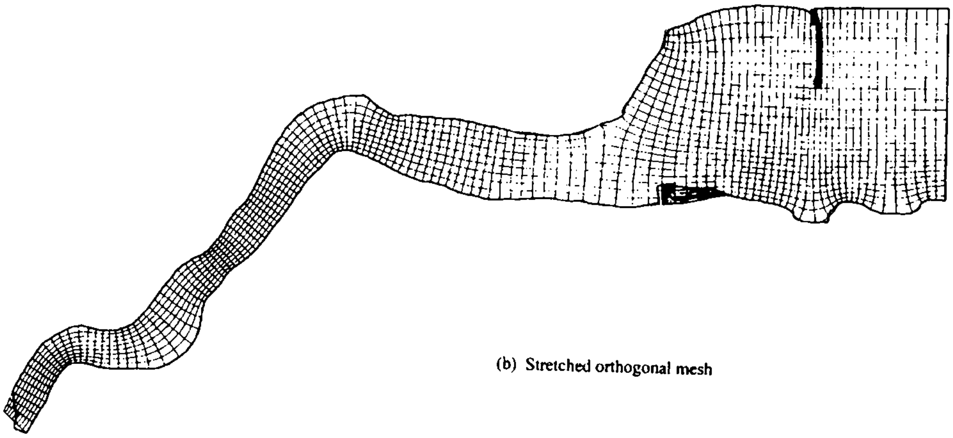

(b) Stretched orthogonal mesh

Figure 13. Boundary-fitted mesh for Humber Estuary

Spurn Head is more accurately represented, (ii) the number of cells across the narrow part of the estuary is increased and (iii) near the outfall site the linear cell size is halved, so that the number of cells is approximately doubled in the ξ-direction.

In order to drive the hydrodynamic model, water elevation data were used at both the seaward and landward boundaries. The water elevation along the North Sea open boundary was evaluated by applying a Coriolis slope similar to equation (21). Simulations were undertaken for spring tides for both the rectilinear and curvilinear models. The predicted velocity fields for a flood tide are presented in Figures 14–16. In the rectilinear model results (Figure 14) the staircase-like mesh and the resultant abrupt changes in velocity direction along the boundary at the upper part of the estuary can be clearly seen. For the curvilinear mesh (Figures 15 and 16) the velocity fields are much better represented in the upper part of the estuary, with the orthogonal model having higher resolutions in the η-direction.

A detailed comparison of the measured water elevations and velocities at various positions and at various tidal states showed an encouraging agreement between predicted and measured results. Figures 17(a) and 17(b) show the water elevation and velocity comparisons at Halton Middle, Middle Shoal and Sunk Channel using the orthogonal mesh. At every site the agreement between the

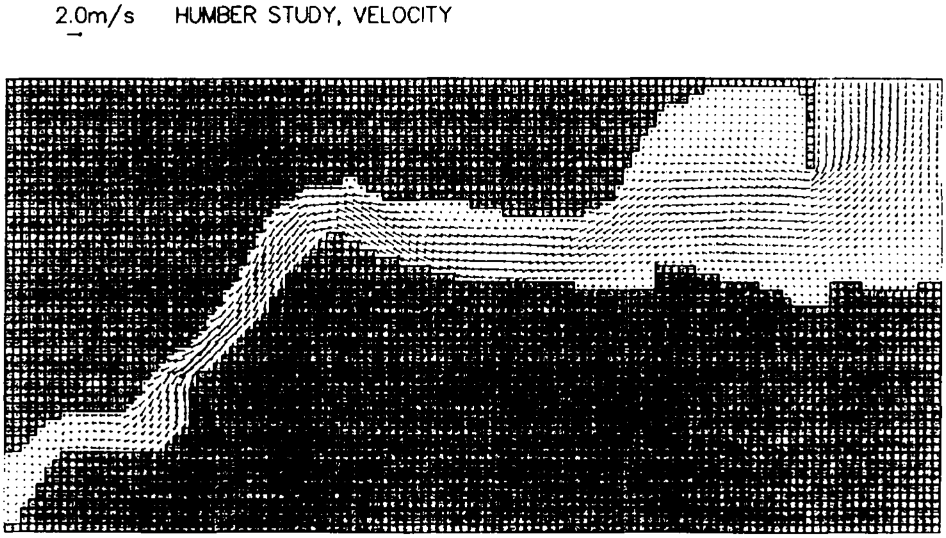

Figure 14. Predicted velocity field using rectilinear mesh

computed and measured results is close for both water elevation and velocity. Since these three sites were relatively far from the boundaries, the differences in results between the curvilinear and rectilinear models are small.

In applying the solute transport model, the transport of a conservative contaminant constantly discharged from the outfall was simulated. The model was first run for four tidal cycles to achieve quasi-steady hydrodynamic conditions before starting to release the contaminant at low water. The contaminant was first flushed upstream during the flood tide and then flushed back during the ebb tide. Figures 18(a) and 18(b) illustrate the concentration distributions after one complete tidal cycle as predicted by the conformal and orthogonal models respectively. Comparing Figures 18(a) and 18(b), it can be seen that with the orthogonal mesh the predicted contaminant field is more concentrated

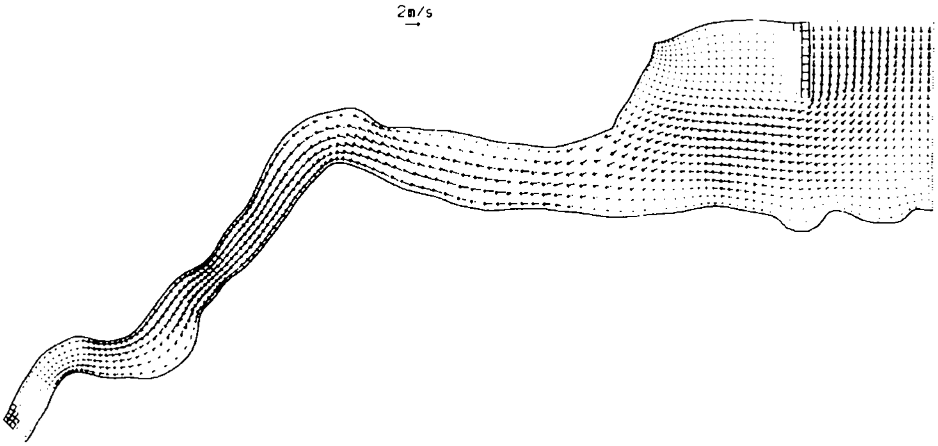

Figure 15. Predicted velocity field using conformal mesh

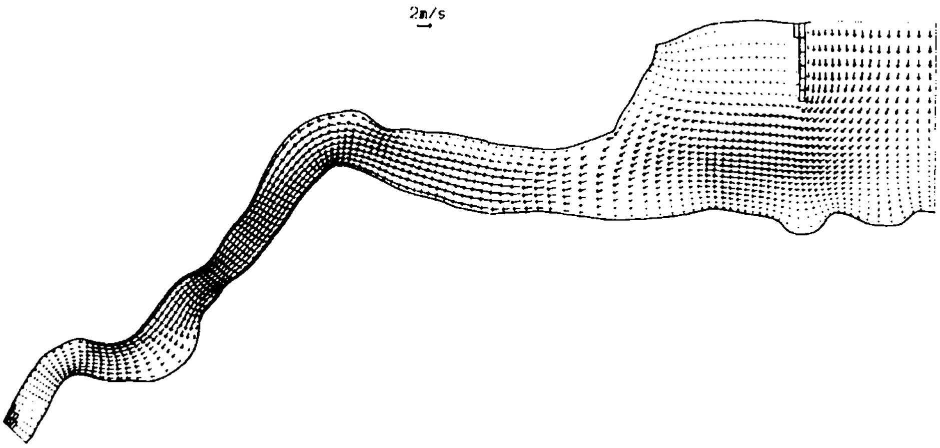

Figure 16. Predicted velocity field using orthogonal mesh

(higher peak value and less spread) near the outfall than it is using the original conformal mesh. This is considered to be the result of the higher mesh resolution near the outfall obtained by the stretching method.

A time step of 180 s was used for the rectilinear model and 90 s for the two curvilinear models, leading to Courant numbers $Cr \approx 6$ for the rectilinear and conformal models and $Cr \approx 9$ for the orthogonal model. The computational time required for five tidal cycles was about 10 min for the rectilinear model, 24 min for the conformal model and 25 min for the orthogonal model using a PC-5100 computer.

The following observations have been made during the numerical tests.

(i) As mentioned in Section 6, a Courant number $Cr \approx 8$ is required for numerical stability, the Courant number being defined in terms of the size of the smallest grid cell.

(ii) Because of this limit on the Courant number, it is usually more expensive to run a curviliner model with the same number of mesh squares owing to the smaller mesh sizes upstream, which require a smaller (global) time step. However, if we achieve the same resolution upstream by reducing the mesh uniformly for the rectilinear model, the increase in computational time is much more substantial. For example, in the current study the linear dimensions of the curvilinear mesh near the landward boundary are about half those of the rectilinear mesh. Thus, if we reduce the mesh size of the rectilinear model to that of the curvilinear model, the computational time will be approximately four times greater if the same time step is used but eight times greater if the time step is also halved to maintain the Courant number.

(iii) Owing to the Courant number constraint, if the stretching method used reduces the mesh size so that the smallest cell is smaller than in the original conformal mesh, then the time step required to run the orthogonal model will be smaller than that for the conformal model. Otherwise the time step will not be affected.

Case study 3

The last test case was to predict steady state velocities and solute transport in a laboratory meandering channel.[27] The flume was 35·4 m long, 2·34 m wide and consisted of two 90° identical

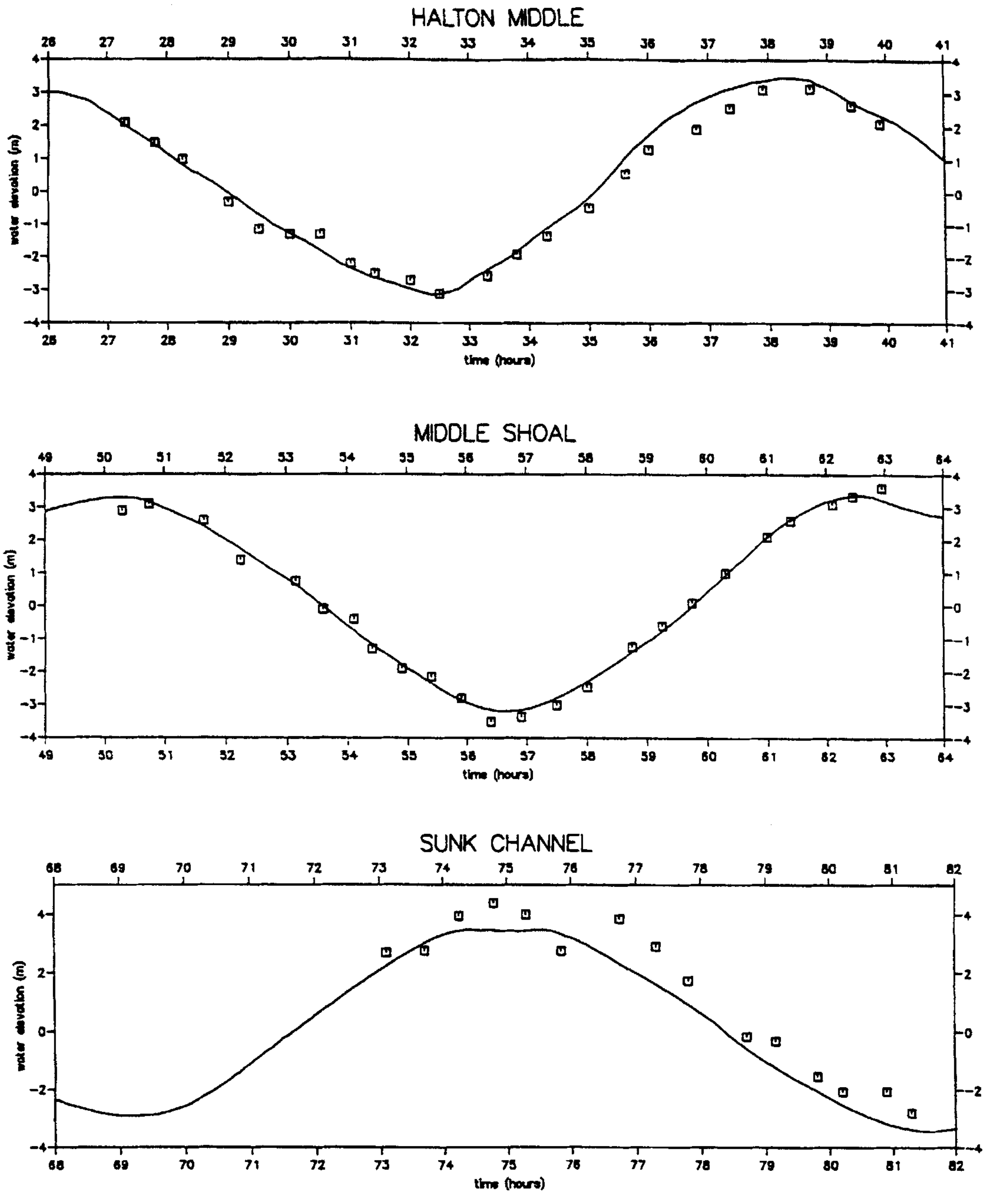

Figure 17(a). Comparison of predicted (—) and measured (□) water elevation for a spring tide using orthogonal model

curves of 8·53 m radius of curvature connected by a 4·27 m straight reach. The depth of the flow was 0·115 m, the slope 0·00035 and the mean velocity 0·305 m s^{-1}.

A boundary-fitted mesh of 103 × 11 grid squares, shown in Figure 19, was generated using the conformal method. The predicted velocity field is shown in Figure 20. It can be seen that the

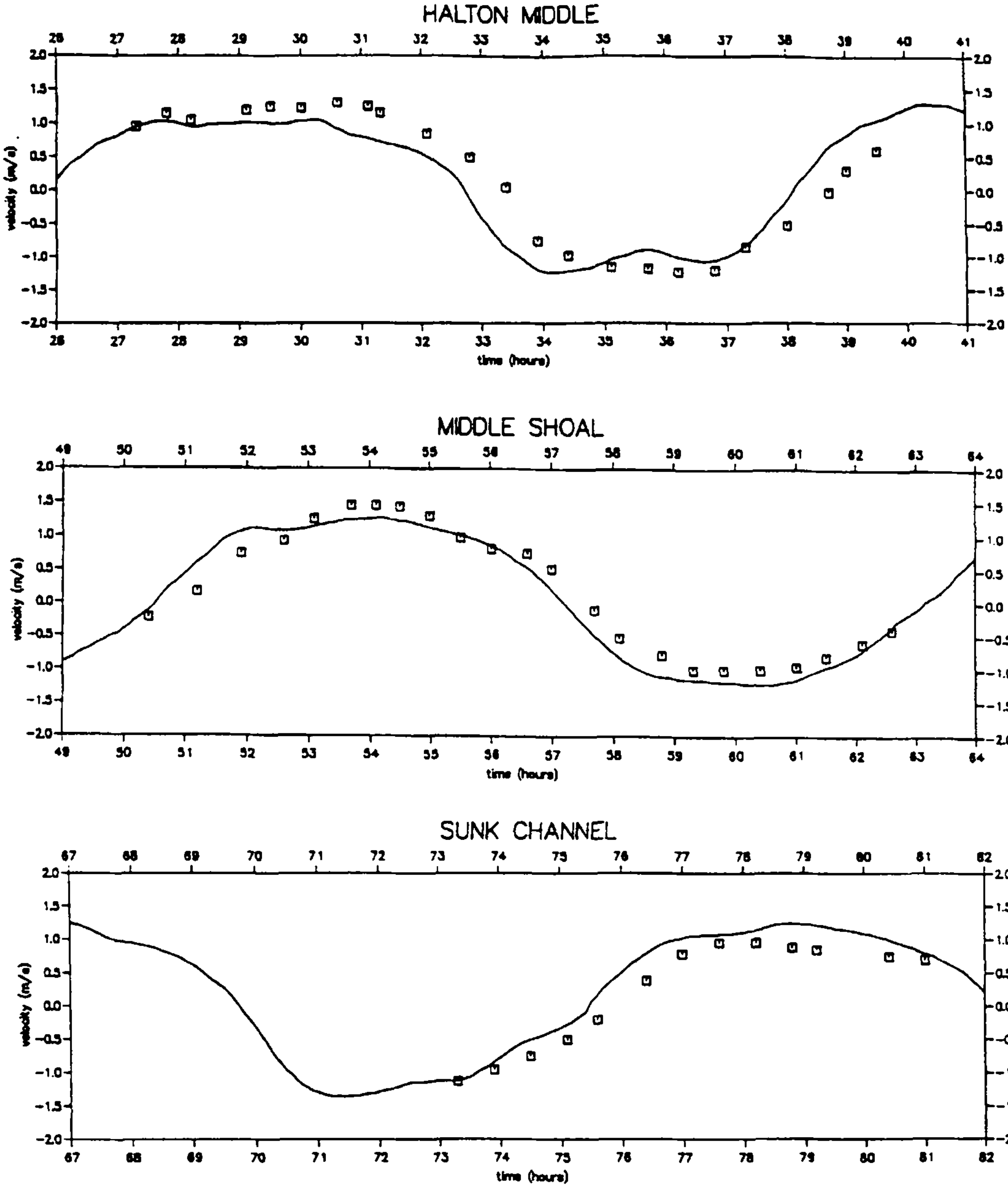

HALTON MIDDLE

MIDDLE SHOAL

SUNK CHANNEL

Figure 17(b). Comparison of predicted (—) and measured (□) velocities for a spring tide using orthogonal model

magnitude of the velocity is increasing from the convex to the concave bank, except in the area very near to the bank, where viscosity is dominant. This is in agreement with the experimental observation undertaken by Chang.[27]

In the three simulations of solute transport shown below, the same flow conditions and source positions as in the experiments were employed; see Figure 21. A constant lateral mixing coefficient of

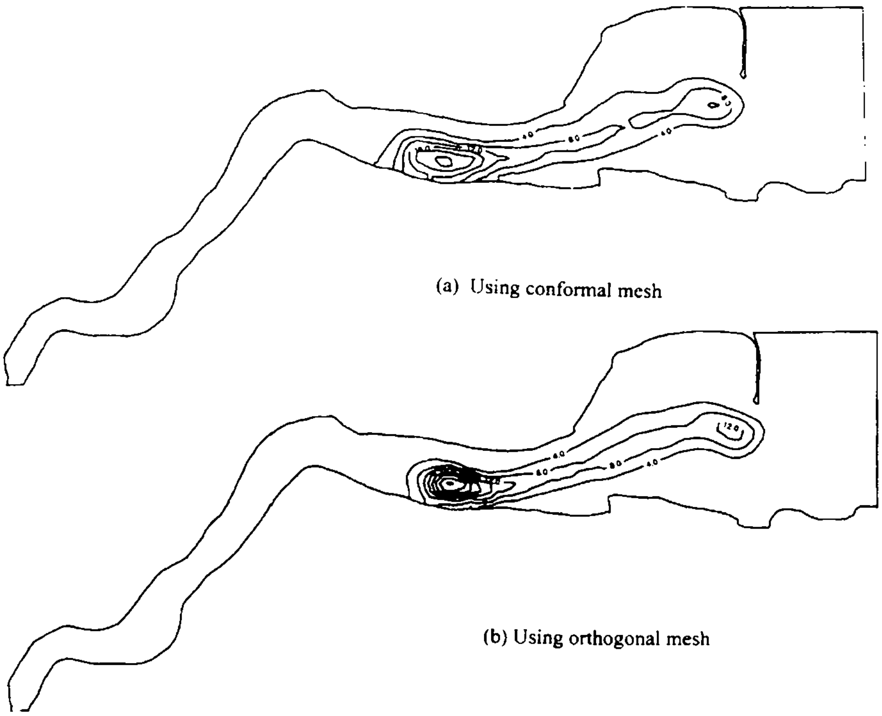

(a) Using conformal mesh

(b) Using orthogonal mesh

Figure 18. Comparison of predicted concentration distributions

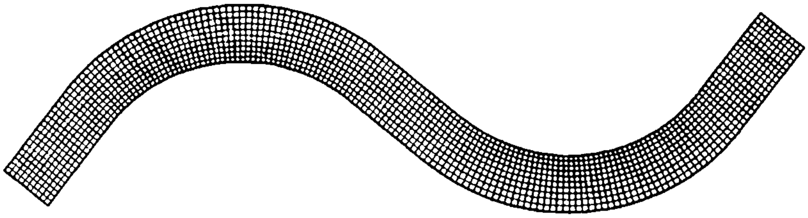

Figure 19. Boundary-fitted mesh for laboratory meandering channel

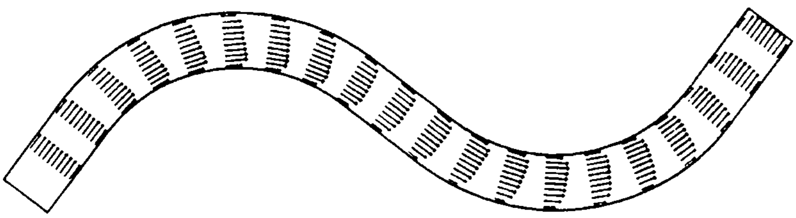

Figure 20. Predicted depth-mean velocity

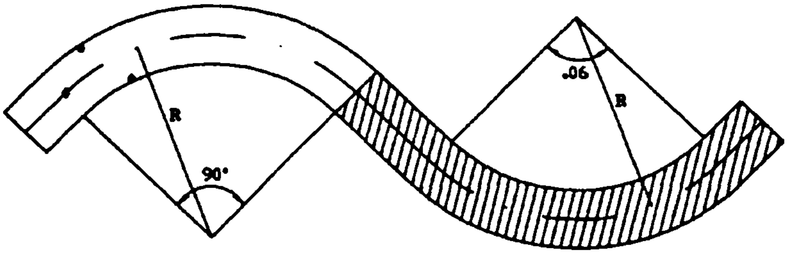

Figure 21. Part of laboratory flume showing working region (shaded) and source positions (dots)

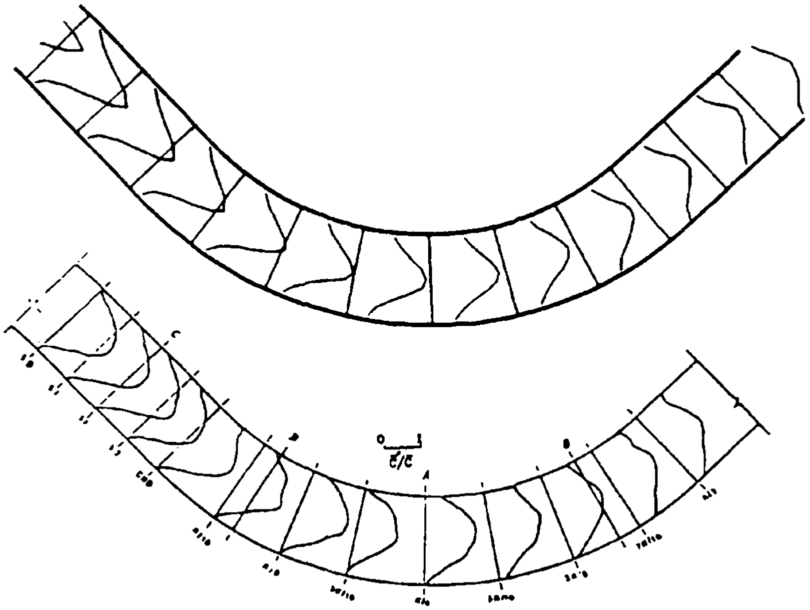

Figure 22. Comparison of predicted and measured solute concentration distributions (source in middle of cross-section)

1·23 was used, as calibrated by Chang[27] from the flume data. Figure 22 shows the comparison between the model simulations and Chang's experiments of depth-mean concentrations when the source is injected into the middle of the flume. Such comparisons generally show good agreement: as usual, the numerically predicted results tend to be smoother than the measurements. Figures 23 and 24 compare experimental measurements and computer simulations when the source was injected along the left bank and right bank respectively. Again these comparisons are very encouraging.

8. CONCLUSIONS

A boundary-fitted curvilinear model for solving the 2D depth-integrated equations of flow and solute transport has been developed. A numerical method for conformal mesh generation has been presented which is able to map a curvilinear polygonal region directly onto a regular polygonal region with horizontal and vertical sides. For cases where a local mesh concentration is required, a stretching technique has been used. The mesh thus generated remains orthogonal but no longer conformal.

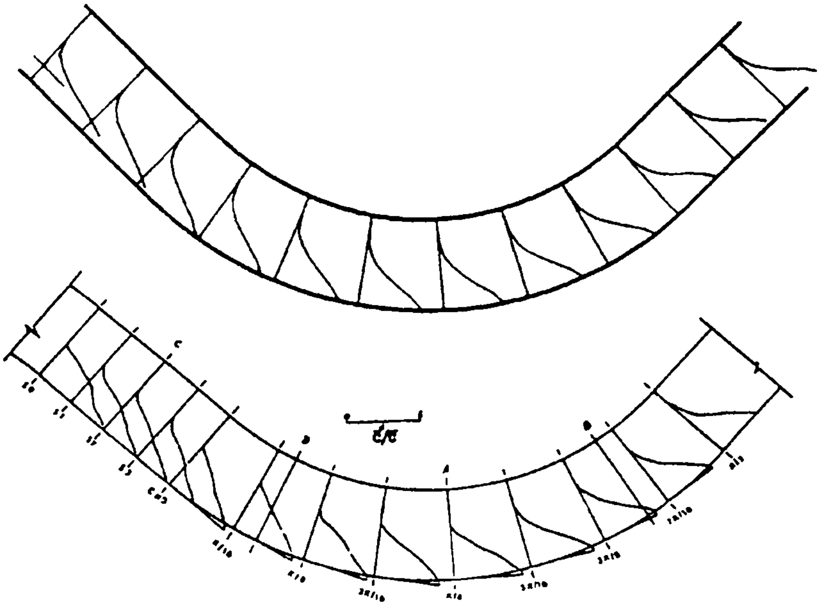

Figure 23. Comparison of predicted and measured solute concentration distributions (source on right-hand side)

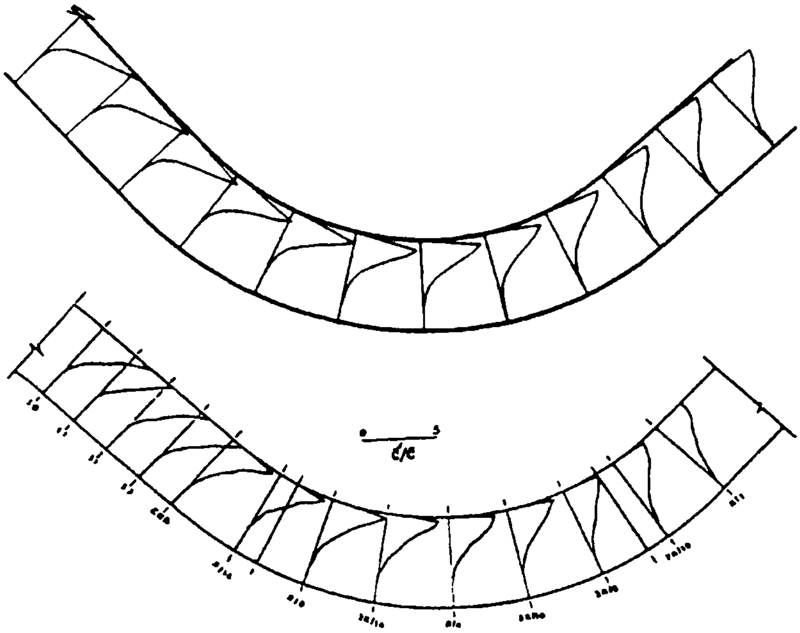

Figure 24. Comparison of predicted and measured solute concentration distributions (source on left-hand side)

A curvilinear hydrodynamic and solute model of estuarine and coastal waters has been developed based on the robust Cartesian co-ordinate model DIVAST. In developing and applying the curvilinear co-ordinate model, emphasis has been given to modelling the complex hydrodynamic processes of practical engineering applications. Since the transformed governing equations (particularly in the case of conformal transformation) are very similar to the original equations in Cartesian co-ordinates, many merits and features of the original model have been maintained in the curvilinear model. Details of the transformed equations and the finite difference schemes used have been given in Sections 5 and 6.

Three case studies have been undertaken to test the model performance. Case studies 1 and 2 tested the ability of the curvilinear model to predict tidal circulation in real estuaries. The predicted results agreed well with measurements in both cases, with no stability problems encountered in these tests. In case study 2, solute transport was also simulated, illustrating the effectiveness of the stretching technique. The final test carried out simulates the solute transport process in a laboratory meandering channel. The comparisons with the flume data are very encouraging.

ACKNOWLEDGEMENTS

This project was funded by the U.K. Engineering and Physical Sciences Research Council under grant GR/F91 704. The authors would like to thank Professor R. A. Falconer, University of Bradford for use of his DIVAST model and for many helpful discussions.

REFERENCES

1. J. J. Leendertse, 'Aspects of a computational model for well mixed estuaries and coastal seas', *RM-5924-Pr*, The Rand Corp., 1967.
2. R. A. Falconer, 'Numerical modelling of tidal circulation in harbours', *J. Waterway, Port, Coastal, Ocean Div., ASCE*, **106**, 31–48 (1980).
3. C. L. Chen and K. K. Lee, 'Great Lakes River-Estuary hydrodynamic finite element model', *J. Hydraul. Eng., ASCE*, **117**, 1531-11550 (1991).
4. M. L. Spaulding, 'A vertically averaged circulation model using boundary-fitted co-ordinates', *J. Phys. Oceanogr.*, **14**, 937–982 (1984).
5. J. Hauser and H. G. Papp, D. Eppel and S. Sengupta, 'Boundary conformal co-ordinate systems for selected two-dimensional fluid flow problems, Part II: Application of the BFG method', *Int. j. numer. methods fluids*, **6**, 529–539 (1986).
6. J. B. T. M. Willemse, G. S. Stelling and G. K. Verboom, 'Solving the shallow water equations with an orthogonal co-ordinate transformation', *Delft Hydraulics Commun.*, **356**, 1986.
7. Y. P. Shen, T. S. Wu aand P. F. Wang, 'Coastal and estuarine hydrodynamic modelling in curvilinear grids', *Proc. 21st Int. Conf. on Coastal Engineering, ASCE*, 1988, pp. 2655–2665.
8. M. A. Gialone, 'Curvilinear long wave hydrodynamic model for tidal circulation and storm surge propagation', in M. L. Spaulding (ed.), Estuarine and Coastal Modelling, Newport, Rhode Island, USA, 1989, pp. 16–26.
9. A. G. L. Borthwick and R. W. Barber, 'River and reservoir flow modelling using the transformed shallow water equations', *Int. j. numer. methods fluids*, **14**, 1193–1217 (1992).
10. J. F. Thompson, Z. U. A. Warsi and C. W. Mastin, *Numerical Mesh Generation: Foundations and Applications*, Elsevier, New York, 1985.
11. R. A. Falconer, 'Flow and water quality modelling in coastal and inland waters', *J. Hydraul. Res., IAHR*, **30**, 437–452 (1992).
12. P. Henrici, *Applied and Computational Complex Analysis*, Vol. III, Wiley, New York, 1986.
13. N. Papamichael, 'Numerical conformal mapping onto a rectangle with applications to the solution of Laplacian problems', *J. Comput. Appl. Math.*, **28**, 63–83 (1989).
14. C. A. Brebbia and J. Dominguez, *Boundary Elements. An Introductory Course*, McGraw-Hill, New York, 1989.
15. S. N. Chandler-Wilde and B. L. Lin, 'A finite difference method for the shallow water equations with conformal boundary-fitted mesh generation', in R. A. Falconer, S. N. Chandler-Wilde and S. Q. Liu (eds), *Hydraulic and Environmental Modelling: Coastal Waters*, Ashgate, Aldershot, Hampshire, 1992, pp. 507–518.
16. J. F. Thompson, Z. U. A. Warsi and C. W. Mastin, 'Boundary-fitted co- ordinate systems for numerical solution of partial differential equations—a review', *J. Comput. Phys.*, **47**, 1–108 (1982).
17. R. A. Falconer, 'A two-dimensional mathematical model study of the nitrate levels in an inland natural basin', *Proc. Int. Conf. on Water Quality Modelling in the Inland Natural Environment*, BHRA, Birmingham, 1986, pp. 325–344.

18. R. A. Falconer, 'Review of modelling flow and pollutant transport processes in hydraulic basins', *Proc. First Int. Conf. on Water Pollution: Modelling, Measuring, and Prediction*, Computational Mechanics Publications, Southampton, 1991, pp. 3–23.
19. S. N. Chandler-Wilde and B. L. Lin, 'Numerical conformal mapping onto arbitrary rectilinear domains', in preparation.
20. R. A. Falconer and Y. P. Chen, 'An improved representation of flooding and drying and wind stress effects in a 2D numerical model', *Proc. Inst. Civil Eng., Part 2, Res. Theory*, **91**, 659–687 (1991).
21. B. P. Leonard, 'A stable and accurate convective modelling procedure based on quadratic upstream interpolation', *Comput. Methods Appl. Mech. Eng.*, **19**, 5–98 (1979).
22. Y. P. Chen and R. A. Falconer, 'Advection–diffusion modelling using the modified QUICK scheme', *Int. j. numer. methods fluids*, **15**, 1171–1196 (1992).
23. British Transport Docks Board, Research Station, 'Humber Estuary sediment flux, Part I: Field measurements', *Rep. 283*, 1980.
24. British Transport Docks Board, Research Station, 'Humber Estuary sediment flux, Part IV: Summary report', *Rep. 290*, 1981.
25. P. H. Owens, 'Mathematical modelling of sediment transport in estuaries', *Ph.D. Thesis*, Department of Civil Engineering, University of Birmingham, 1986.
26. Cahyono, 'Three-dimensional numerical modelling of sediment transport processes in non-stratified estuarine and coastal waters', *Ph.D. Thesis*, University of Bradford, 1993.
27. Y. Chang, 'Lateral mixing in meandering channels', *Ph.D. Thesis*, Department of Mechanics and Hydraulics, University of Iowa, 1971.